electronics

MDPI

Article

A Three-Port DC-DC Converter with Partial Power Regulation for a Photovoltaic Generator Integrated with Energy Storage

Donghui Ye and Sergio Martinez *

Department of Electrical Engineering, Escuela Técnica Superior de Ingenieros Industriales, Universidad Politécnica de Madrid, 28006 Madrid, Spain; donghui.ye@alumnos.upm.es
* Correspondence: sergio.martinez@upm.es

Abstract: A novel integrated DC-DC converter is proposed for the first stage of two-stage grid connected photovoltaic (PV) systems with energy storage systems. The proposed three-port converter (TPC) consists of a buck–boost converter, interposed between the battery storage system and the DC-AC inverter, in series with PV modules. The buck–boost converter in the proposed TPC is utilized for maximum power point tracking by regulating two power switches. The output power of the proposed converter is regulated by controlling the DC-AC converter. During the battery-charging mode, partial power regulation is employed with a direct power flow path (the series-connection of the PV panel, the battery and the output). As resistances in this path are almost negligible, the power conversion efficiency is higher than existing topologies. During battery-discharging mode, the power conversion is processed through a buck–boost converter with only two active power switches and one inductor. With fewer components, higher power conversion efficiency is also achieved. The circuit operation and analysis are presented in detail. To illustrate the simplicity of the converter control, the performance of the converter is tested with a straightforward maximum power point tracking on a PV system with battery cells. Simulation and experimental tests are carried out to demonstrate circuit operation and power conversion efficiency.

Keywords: battery storage system; buck–boost converter; partial power regulation; PV system; three-port converter

Citation: Ye, D.; Martinez, S. A Three-Port DC-DC Converter with Partial Power Regulation for a Photovoltaic Generator Integrated with Energy Storage. *Electronics* **2024**, *13*, 2304. https://doi.org/10.3390/electronics13122304

Academic Editors: Irfan Ahmad Khan and Ghulam Abbas

Received: 26 April 2024
Revised: 8 June 2024
Accepted: 10 June 2024
Published: 12 June 2024

1. Introduction

Photovoltaic (PV) power is becoming increasingly important in many applications, such as LEDs, DC motors and power systems, due to its environmental advantages, the maturity of manufacturing technologies and the low costs in operation [1–6]. However, the main disadvantage of PV power is that the generated power is uncertain, being highly dependent on weather conditions. To utilize PV power in an efficient way, hybridization with battery energy storage systems (BESSs) is commonly introduced to avoid energy waste and fulfill output requirements.

Conventionally, two individual DC-DC power converters are used in grid-connected PV systems with battery packs [7–11]. One of them is connected to the PV modules to implement maximum power point tracking (MPPT) and to adapt the power generated by solar panels to the grid requirements. The other DC-DC converter is connected to the battery packs to complement the power required by the grid or to store PV power, depending on the operation mode. Figure 1 shows the power flow paths of the traditional configuration with two individual DC-DC converters. Due to the use of an additional DC-DC converter, connected to the battery packs, more components are used, resulting in low efficiency of the whole PV system, low power density and high costs [12].

To face these issues, some circuit topologies with three-port converters (TPCs), instead of two individual DC-DC converters, have been proposed [13–16]. Figure 2a shows the power flow paths of traditional TPCs. They can be categorized into three types: isolated [15,16], partly isolated and non-isolated TPCs [13]. For isolated TPCs, multi-winding

transformers with a group of active power switches are required to provide galvanic isolation between ports and to achieve high voltage gain [17]. However, due to the employment of transformers and a group of switches, the volume and the costs increase [18–21]. As there are some applications in which not all ports need to be isolated, partly isolated TPCs can be used, thus allowing for higher power density and smaller volume [22,23]. In other applications in which the galvanic isolation is not needed, non-isolated TPCs are used, with the advantages of even higher efficiency, higher power density, smaller size, lower costs and simpler control, compared to the other two types of TPCs [24–26]. In [27,28], some TPCs are proposed for non-isolated high voltage gain applications with detailed circuit operation analysis. As presented in [27], the topology has the advantage of high voltage gain without the use of transformer and lower voltage stresses on switches. In [28], a higher voltage gain is achieved without the need for coupled inductors and voltage multiplier cells. Nevertheless, in [27,28], a number of components (including switches, capacitors, transformers, and inductors) are used, resulting in higher control complexity, lower efficiency and higher costs. As presented in [29], a soft switching TPC is proposed with zero-voltage switching (ZVS) and leakage inductor energy recycling. However, the complexity of the control increases with the number of power switches and an active clamp circuit.

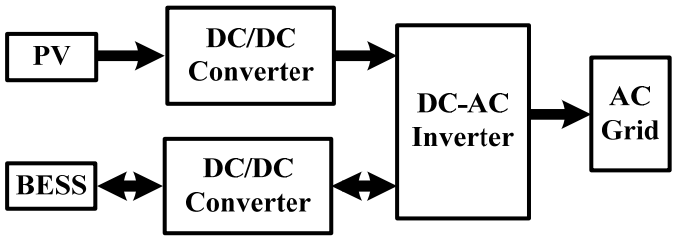

Figure 1. Power flow paths of a traditional configuration of a PV generator with BESS, using two power converters.

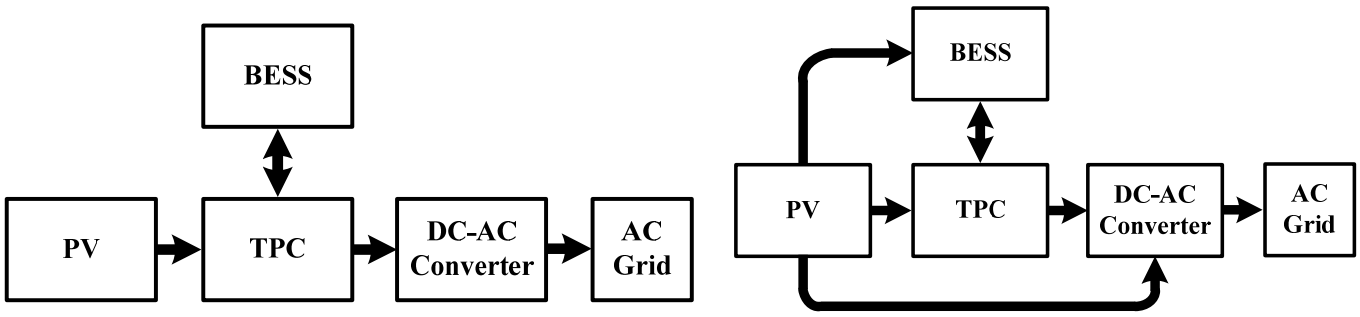

Figure 2. Power flow paths of (**a**) traditional TPC and (**b**) proposed TPC with PPR.

This paper presents the investigation of an alternative approach, namely a battery-integrated step-down TPC with partial power regulation (PPR) [30,31] for the first stage of two-stage PV systems. Figure 2b shows the power flow paths of the proposed TPC. Compared with a fully rated traditional TPC, only a fraction of the PV power is processed by the TPC, reducing power losses in the components. In addition, only two power switches and one inductor are used in the proposed TPC, thus improving power conversion efficiency and power density, reducing the costs, and allowing for simpler control. Moreover, due to the adoption of PPR technology in battery-charging mode, the power conversion efficiency is further increased. Table 1 shows the comparison between the proposed topology and other non-isolated TPCs. As can be seen in this table, less components are used, and higher efficiency is achieved.

Table 1. Comparison between the proposed topology and other TPCs.

Topology	Diodes	Inductors	Switches	Capacitors	Rated Power (W)	Efficiency (%)
[24]	5	2	3	4	100	91–94
[25]	2	2	2	2	100	85–94
[26]	5	1	4	3	50	87.8–93
[27]	1	2	4	4	1000	96–98
[28]	5	2	3	4	200	86–99
[29]	2	1	5	3	300	94.2–96.8
Proposed	0	1	2	3	15	95.4–99.68

In summary, the main contribution of this proposal is a novel topology of a PPR TPC with the following advantages:

1. Few components (two power switches, one inductor and three capacitors) are used in the proposed non-isolated TPC so that the costs and size are reduced;
2. With only two synchronous rectification power switches, the proposed topology can be easily controlled, and the control strategy can be simplified;
3. With the use of a direct power flow path while in charging mode, the power conversion efficiency is increased.

The paper is organized as follows. Section 2 presents the proposed circuit configuration. Section 3 analyzes the circuit steady state operation in its different operation modes. Section 4 describes one possible control strategy. Section 5 presents simulation and experimental results. Finally, Section 6 summarizes the conclusions.

2. Circuit Configuration

Figure 3 shows the circuit configuration of the proposed TPC, including a unidirectional input port (from the PV panels), a bidirectional input/output port (from/to the battery) and a unidirectional output port (to the DC-AC inverter). The power from the unidirectional input port, which could be fed with renewable energy, such as the solar PV panels shown in Figure 3, supplies energy to the output ports. The bidirectional input/output port, connected with energy storage elements, such as BESSs and/or supercapacitor banks, could be used as an input or an output port, depending on whether it supplies power to the unidirectional output port or obtains the energy from the unidirectional input port. The unidirectional output port is connected to a DC-AC inverter in AC grid-connected applications.

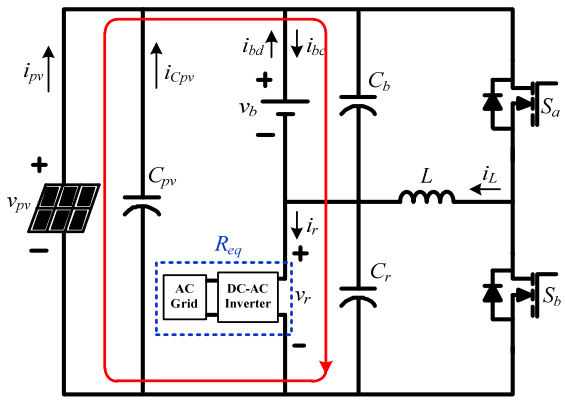

Figure 3. Circuit configuration of the proposed topology with direct power flow path (red line).

The PV module is connected to the battery cell and the DC-AC inverter in series, creating a direct power flow path (red line in Figure 3) that improves the power conversion efficiency. A buck–boost converter, consisting of two power switches S_a and S_b, an inductor L, and two capacitors C_b and C_r, is connected between the battery and the DC-AC inverter.

With such a configuration, the PV voltage v_{pv} is the sum of the voltages on the battery v_b and the input of the DC-AC inverter v_r. As a DC voltage source, v_b is held almost constant at the steady state operation in a high-frequency cycle. Thus, the maximum power point (MPP) of the PV module can be found by regulating v_r. However, during long-term operation, v_r varies due to the fact that the voltage of MPP highly depends on weather conditions and v_b depends on the state of charge (SOC) of the battery. This means v_r depends on the voltage of MPP and v_b. But the current i_r in the DC-AC inverter can be regulated by the adjustment of the DC-AC inverter to cope with the grid power requirements.

3. Circuit Steady State Operation and Analysis

The contribution of this work is the TPC with PPR, irrespective of its connection to a DC-AC inverter or to any other power consumption. Thus, for the simplicity of the analysis, in what follows, the output port is supposed to be connected to an equivalent variable resistance R_{eq} instead of the DC-AC inverter.

The proposed circuit may be operated at either continuous conduction mode (CCM) or discontinuous conduction mode (DCM), depending on the designed circuit parameters and operating conditions. The circuit operation can be divided into six modes. To simplify the analysis, all components in the proposed TPC are assumed to be ideal, the capacitors are large enough to maintain the voltage constant and, as stated, the variable resistance R_{eq} symbolizes the load of the PV system.

- Mode I

In Mode I, the load and the battery are both supplied by solar energy. As only a small amount of the power is processed by the buck–boost converter, it may be operated in CCM or DCM. Figure 4 depicts three operation stages of the proposed TPC in this mode.

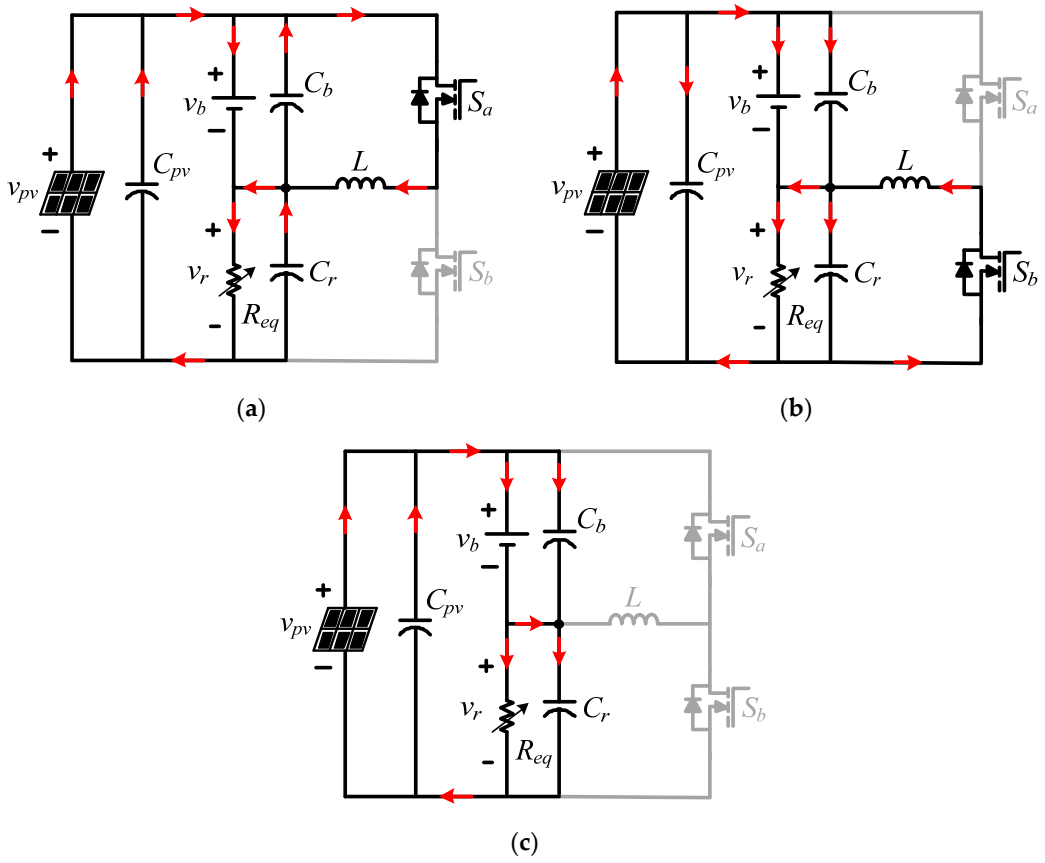

Figure 4. Operation stages of Mode I, when PV module supplies energy to the load and the battery: (**a**) Stage I-1; (**b**) Stage I-2; and (**c**) Stage I-3.

Stage I-1 (t_0, t_1)

Stage I-1 starts when the power switch S_a is turned ON. The inductor L is charged by the PV module. The inductor current i_L increases linearly with the following slope:

$$\frac{di_L}{dt} = \frac{V_b}{L} \tag{1}$$

Part of the power generated by the PV module is delivered to the load and the battery directly. This stage ends when S_a is switched OFF.

Stage I-2 (t_1, t_2)

In stage I-2, S_a is turned OFF and S_b is switched ON to conduct i_L. The energy stored in the inductor L is released to the load with the following slope:

$$\frac{di_L}{dt} = -\frac{V_{pv} - V_b}{L} \tag{2}$$

Stage I-2 ends when S_a is switched on again or i_L declines to zero. The operation enters stage I-3 if i_L decreases to zero. In case S_a is switched on before i_L reaches zero, the operation returns to stage I-1.

Stage I-3 (t_2, t_3)

During stage I-3, both S_a and S_b are turned OFF. The power generated by the PV module is supplied to the battery and the load in a straight manner. When S_a is turned ON, the circuit operation goes back to stage I-1 of the next switching cycle.

In Mode I, the power conversion efficiency can be expressed as follows:

$$\eta = (p_b + p_r)/p_{pv} \tag{3}$$

where p_b is the battery power, p_r is the load power and p_{pv} is the PV power.

- Mode II

In Mode II, both the PV module and the battery supply energy to the load. All the power generated by the PV module and the battery is transferred to the load through a buck–boost converter which is designed at CCM. The circuit operation can be divided into two stages, as shown in Figure 5.

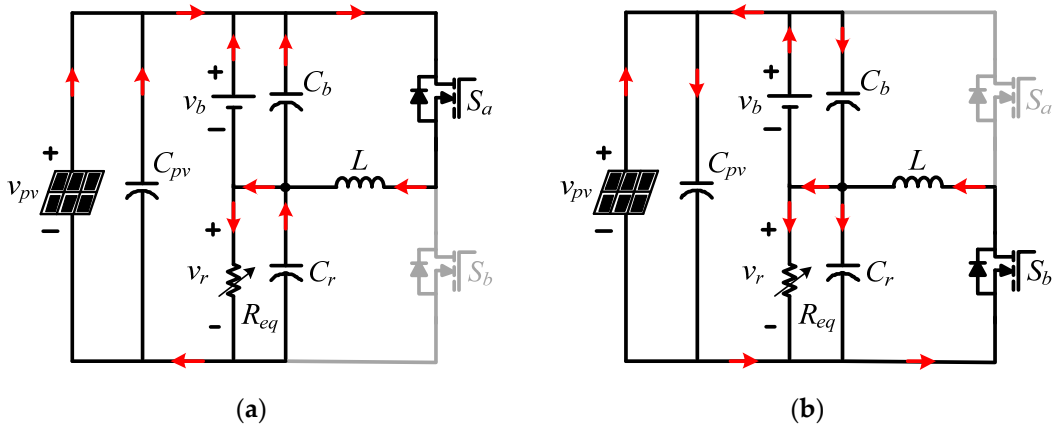

Figure 5. Operation stages of Mode II, when the PV module and battery supply energy to the load: (**a**) Stage II-1 and (**b**) Stage II-2.

Stage II-1 (t_0, t_1)

Stage II-1 starts when S_a is turned ON. L is charged by the PV module and the battery with an increasing current i_L (1). This stage ends when S_a is switched OFF.

Stage II-2 (t_1, t_2)

During stage II-2, S_b is switched ON. The load voltage is applied to L, resulting in a decrease in i_L with a slope defined by (2). Stage II-2 ends when S_a is turned ON again.

In Mode II, the power conversion efficiency can be expressed as follows:

$$\eta = p_r / (p_b + p_{pv}) \tag{4}$$

- Mode III

In this mode, the average PV power is approximately equal to the load power. In practice, the current ripple on the battery cannot be eliminated, but can be reduced by using some techniques [32]. In this work, a capacitor is connected in parallel with the battery to reduce current ripple. The circuit is designed to be operated in Mode III when the average battery current is approximately equal to zero. During this mode, the battery is both charged and discharged in a switching cycle. Its operation is between Mode I and Mode II.

In Mode III, the power conversion efficiency can be expressed as follows:

$$\eta = p_r / p_{pv} \tag{5}$$

The relationship among the PV voltage v_{pv}, the battery voltage v_b, and the load voltage v_r, during Modes I, II and III, can be expressed as follows:

$$v_{pv} = v_b + v_r \tag{6}$$

The load voltage is regulated by the buck–boost converter. Then, the load voltage can be expressed as follows:

$$v_r = \frac{d}{d'} v_b \tag{7}$$

where d is the duty ratio of the power switch S_a, and d' is the duty ratio for the inductor current, decreasing from its peak to zero in a switching cycle. For CCM operation, the sum of d and d' is equal to 1.

Substituting (7) into (6) yields

$$v_{pv} = \left(1 + \frac{d}{d'}\right) v_b \tag{8}$$

Thus, the MPPT can be implemented by adjusting d.

- Mode IV

In case the BESS is fully charged, exhausted or with unexpected damage, circuit operation enters Mode IV. The PV power is equal to the load power and the battery needs to be isolated (the switch is not shown in the figures). The proposed circuit is operated as a buck converter. The circuit operation with CCM can be divided into two stages, as shown in Figure 6.

Stage IV-1 (t_0, t_1)

Stage IV-1 begins when S_a is turned ON. The PV module supplies energy to L and the load. The inductor current i_L increases linearly with the following slope:

$$\frac{di_L}{dt} = \frac{V_{pv} - V_r}{L} \tag{9}$$

This stage ends when S_a is switched OFF.

Stage IV-2 (t_1, t_2)

In stage IV-2, S_b is turned ON to conduct the inductor current i_L. L supplies the stored energy to the load with the following slope:

$$\frac{di_L}{dt} = -\frac{V_r}{L} \tag{10}$$

When S_a is turned ON, stage IV-2 ends.

In Mode IV, the power conversion efficiency is given by (5). The circuit performs as a buck converter. The PV voltage can be expressed as follows:

$$v_{pv} = \left(1 + \frac{d'}{d}\right) v_r \tag{11}$$

- Mode V

Mode V corresponds to the case in which the load does not require any power. Figure 7 illustrates two operation stages of the proposed topology in this mode.

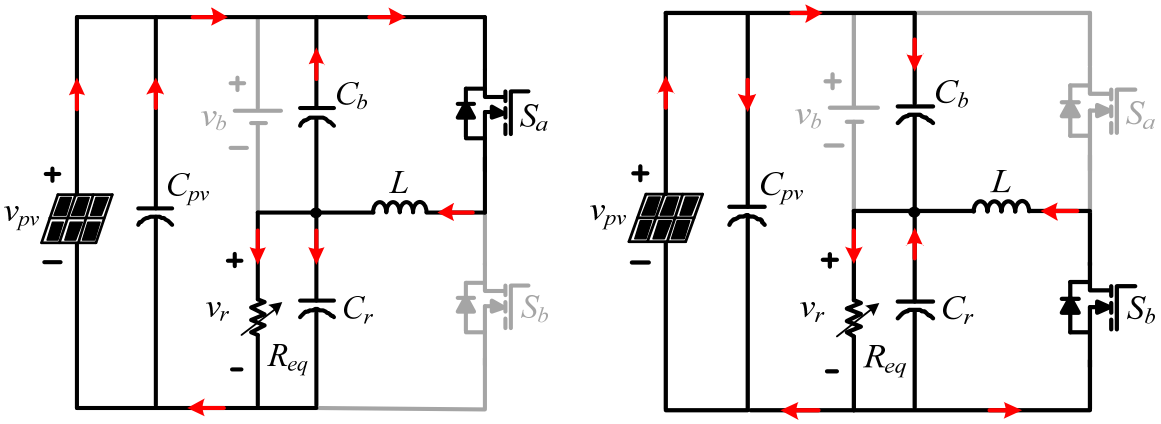

Figure 6. Operation stages of Mode IV, when the PV power is equal to the load power and the battery needs to be isolated: (**a**) Stage IV-1 and (**b**) Stage IV-2.

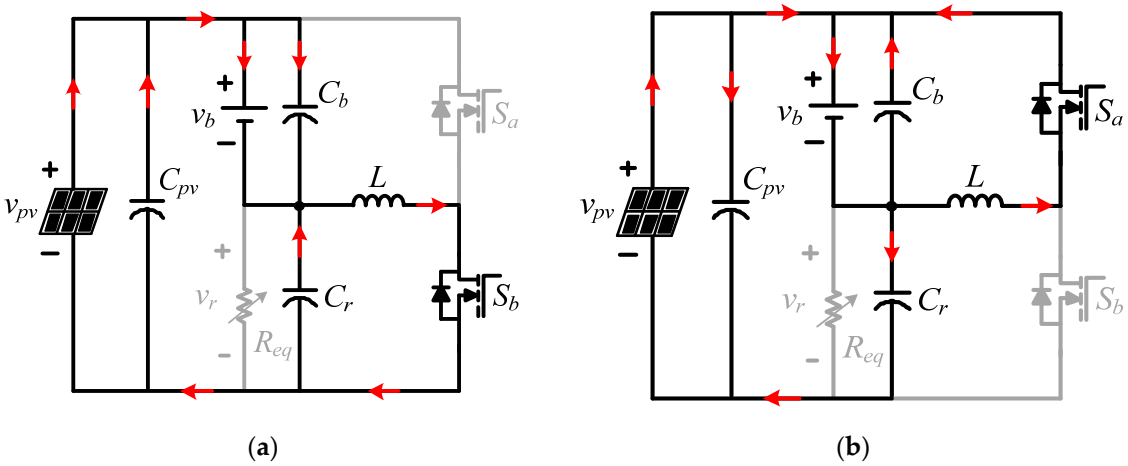

Figure 7. Operation stages of Mode V, when the PV module supplies energy to the battery: (**a**) Stage V-1 and (**b**) Stage V-2.

Stage V-1 (t_0, t_1)

In stage V-1, S_b is turned ON. The inductor L is supplied by the PV module, resulting in an increase in i_L with the following slope:

$$\frac{di_L}{dt} = \frac{V_{pv} - V_b}{L} \tag{12}$$

This stage ends when S_b is switched OFF.

Stage V-2 (t_1, t_2)

In stage V-2, S_b is turned OFF and S_a is switched ON to conduct the inductor current i_L. L supplies the stored energy to the battery with the following slope:

$$\frac{di_L}{dt} = -\frac{V_b}{L} \tag{13}$$

When S_b is switched ON, the circuit enters stage V-1 of the next frequency cycle.

In this mode, the battery is charged by the PV module. The relationship between v_{pv} and v_b is given by (8). The power conversion efficiency can be expressed as follows:

$$\eta = p_b / p_{pv} \tag{14}$$

- Mode VI

During Mode VI, the sunlight is insufficient to generate any energy for the load. All load power is supplied by the battery through a buck–boost converter with CCM operation. Figure 8 shows the two operation stages of this mode.

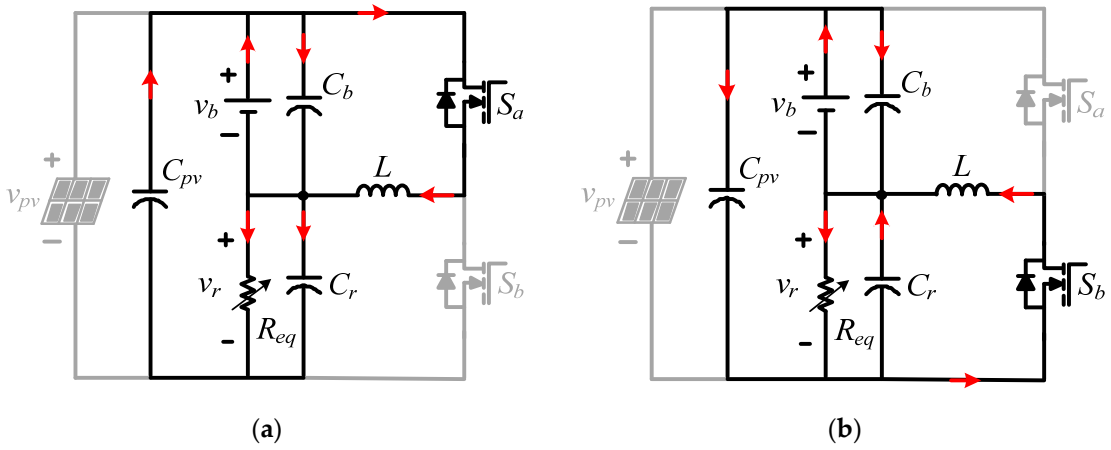

Figure 8. Operation stages of Mode VI, with just the battery supplying energy to the load: (**a**) Stage VI-1 and (**b**) Stage VI-2.

Stage VI-1 (t_0, t_1)

Stage VI-1 starts when S_a is turned ON. The battery supplies energy to L and the capacitor C_{pv} releases energy to the load. i_L increases linearly with a slope defined by (1). This stage ends when S_a is switched OFF.

Stage VI-2 (t_1, t_2)

In stage VI-2, S_a is turned OFF and S_b is turned ON to conduct the inductor current i_L. The load voltage v_r on L leads to a decrease in its current with a slope defined by (10). This stage ends when S_a is turned ON again.

During Mode VI, the relationship between v_b and v_r is given by (7). The power conversion efficiency can be expressed as follows:

$$\eta = p_r / p_b \tag{15}$$

4. Control Strategy

To illustrate the simplicity of the control of the proposed TPC with PPR, the performance of the converter is tested with a straightforward MPPT on a PV system with battery cells. Figure 9 shows the control flow chart of the system with load power regulation. At the beginning, the PV voltage v_{pv}, the PV current i_{pv}, the load current i_r, the PV voltage

v_r, the battery voltage v_b, and the battery current i_b are measured by current and voltage detection circuits, which are shown in Figures 10 and 11, respectively. In practice, the measured voltages (v_{pv}, v_r and v_b) and the currents (i_{pv}, i_r and i_b) are too high for the micro-controller (in this case, a TEXAS INSTRUMENTS TMS320F28335 one), and thus, must be reduced to the accepted signal levels. The current is sensed by a Hall-effect sensor, yielding a corresponding voltage v_s, and then transmitted into a current sampling circuit, which is built by an operational amplifier (OPA) to reduce the signal level, with a voltage reference v_{ref}. The output voltage v_{co} of the current sampling circuit is transferred to the micro-controller through a low-pass filter and a voltage follower to reduce high-frequency noise. The relationship between v_s and the output of the current detection circuit v_{io} is expressed as follows:

$$v_{io} = \left(v_s - v_{ref}\right)\frac{R_2}{R_1} \tag{16}$$

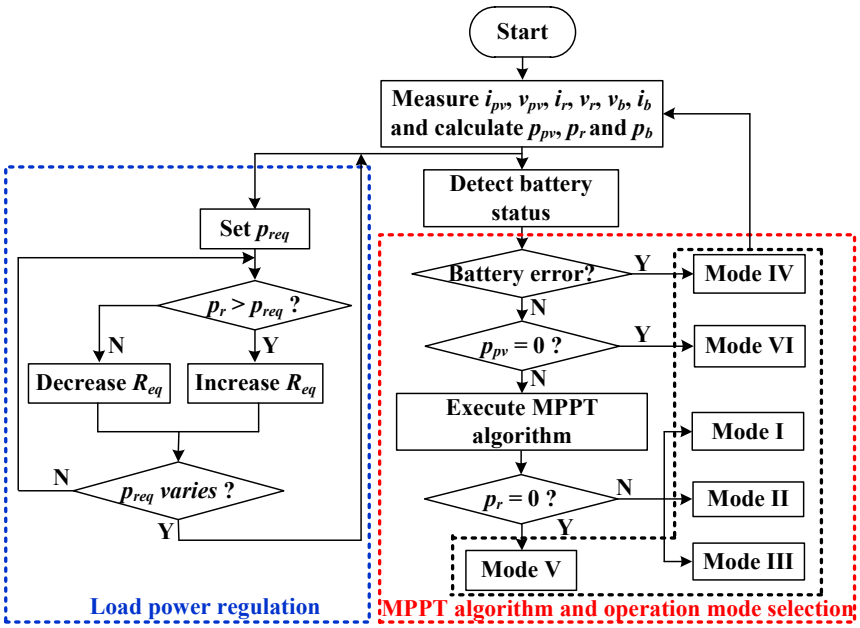

Figure 9. Control flow chart with load power regulation, perturb and observe MPPT algorithm, and operation mode selection.

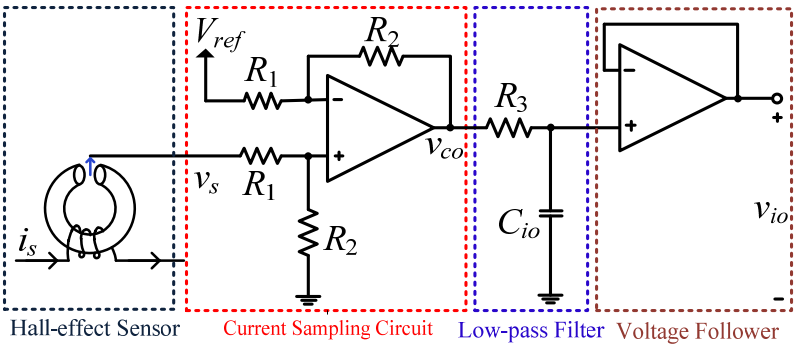

Figure 10. Current detection circuit.

For the voltage detection circuit shown in Figure 11, the measured voltage v_{vin} is detected with a voltage-sampling circuit and then passed through a low-pass filter and a voltage follower into the micro-controller to execute the control strategy. The relationship between v_{vin} and v_{vo} is expressed as follows:

$$v_{vo} = v_{vin}\frac{R_5}{R_4} \tag{17}$$

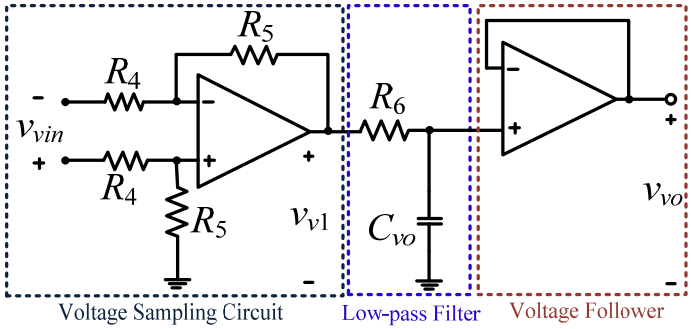

Figure 11. Voltage detection circuit.

From the current and voltage measurements, the PV power p_{pv}, the load power p_r, and the battery power p_b are calculated. Then, the battery status is obtained. When an abnormal battery situation is detected, the circuit operation enters Mode IV. If the battery is healthy and the irradiance is not enough for the PV panel to generate any power, Mode VI is entered. If the power generated by the PV module is above zero, the MPPT algorithm (a perturbation and observation (P&O) algorithm is used in this work) is executed to avoid energy waste. Then, the operation mode is selected by the comparison of the load power and the PV power. If the load is equal to zero, the circuit is operated in Mode V. If the load is above zero, operation Mode I, II or III is selected, depending on the power generated by the PV module.

At the same time, the load power regulation is executed independently to maintain the load power constant. After the calculation of the load power p_r, the required load power p_{req} is set. When p_r is higher than p_{req}, the resistance of the equivalent variable resistor R_{eq} increases. On the contrary, R_{eq} decreases if p_r is lower than p_{req}.

5. Simulation and Experimental Results

A simulation model for a PV system with a battery is set up in Simulink (10.6 (R2022b)), as shown in Figure 12, to verify the circuit operation of the proposed topology and the effectiveness of the control strategy. The circuit parameters are listed in Table 2. The PV system employs a solar panel with a rated maximum output power of 28 W at 1000 W/m^2 and 25 °C. The proposed converter is designed to be operated in CCM when the load power is at 15 W. The conduction resistance of MOSFETs simulates the conduction losses, while the losses on the inductor L are simply simulated with an equivalent series resistance R_L.

Table 2. Circuit parameters.

Parameters	Value
Rated PV power, p_{rpv}	28 W
Open circuit voltage, V_{oc}	22 V
Short-circuit current, I_{sc}	1.69 A
Voltage at maximum power point, V_{mp}	17.3 V
Current at maximum power point, I_{mp}	1.645 A
Nominal battery voltage, v_N	7.4 V
Nominal battery capacity, SOC_N	4.6 Ah
Switching frequency, f_s	25 kHz
Inductance of inductor, L	180 µH
Filter capacitors, C_{pv}, C_b, and C_r	470 µF
Conduction resistance of MOSFETs, R_{on}	4.5 mΩ
Inductor equivalent serial resistance, R_L	25 mΩ

To avoid energy waste and regulate the load power, the MPPT with a P&O algorithm and load power regulation are implemented simultaneously. The instantaneous output voltage and current of the PV module and the voltage and current on the variable resistor detected by the measurement blocks are transferred to a MATLAB (R2022b Update 5

9.13.0.2193358) function block to execute the MPPT algorithm and select operation mode, giving a duty ratio as an output. This duty ratio feeds a PWM generator to produce complementary PWM signals PWM_{sa} and PWM_{sb} to drive the MOSFETs. Simple load power regulation is used to adjust the resistance of the variable resistor to maintain the load power at constant level.

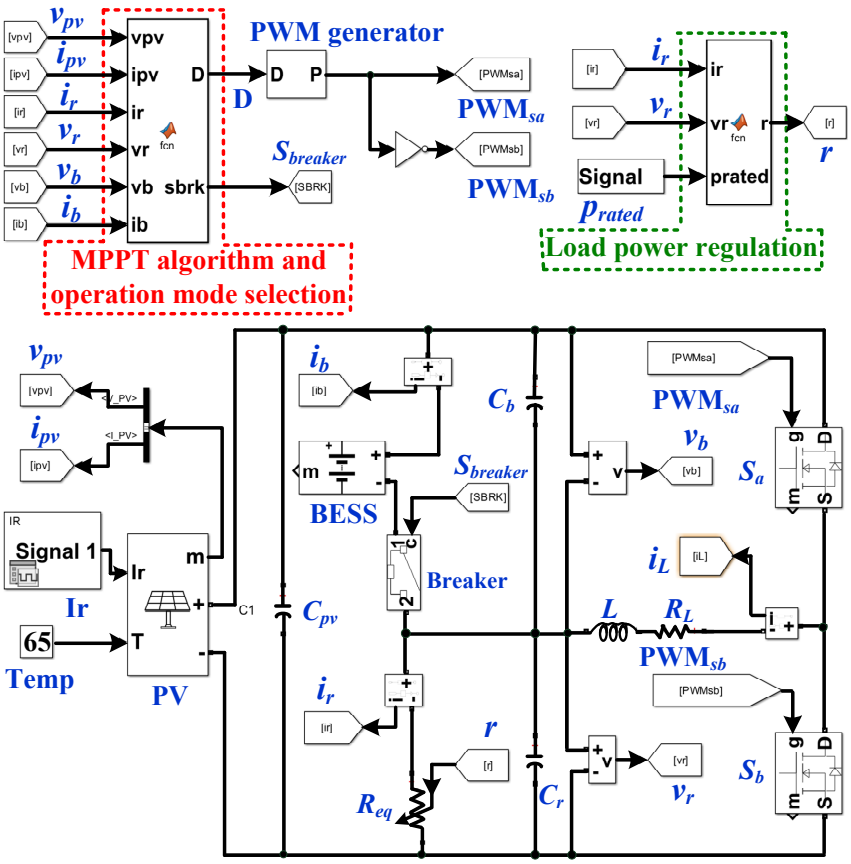

Figure 12. PV system Simulink model with the proposed circuit.

Figure 13 shows simulation key waveforms at steady-state operation with different operation modes. The PV system is operated at 1000 W/m^2, 65 °C and Mode I in Figure 13a. The PV voltage and current are regulated around 15.3 V and 1.64 A, respectively. The battery is charged by the PV module with an average charging current of 1.24 A. The battery voltage is held almost constant at 8.09 V. The load power is approximately equal to 15 W with a resistor R_{eq} = 3.74 Ω. The inductor is operated at CCM with a peak current of 1.25 A.

Figure 13b illustrates an example of a PV power lower than the load power. The PV system is operated at Mode II with irradiance of 400 W/m^2. The energy stored in the battery is released to the load. The load power remains at 15 W and the PV power is regulated at an MPP of 10.14 W. The peak inductor current is 3.09 A.

When the PV system is operated at 600 W/m^2, the average battery current is approximately equal to zero, as shown in Figure 13c. The circuit operation enters mode III. The battery is charged and discharged in a switching cycle from t_0 to t_2. The peak inductor current reaches 2.6 A.

Figure 13d shows a case with an abnormal battery state, in which Mode IV is implemented. The battery is isolated, resulting in a PV power of 20.21 W with irradiance of 800 W/m^2.

In the case that only the PV module supplies energy to the battery (Mode V) with irradiance of 800 W/m^2, the simulation key waveforms are shown in Figure 13e.

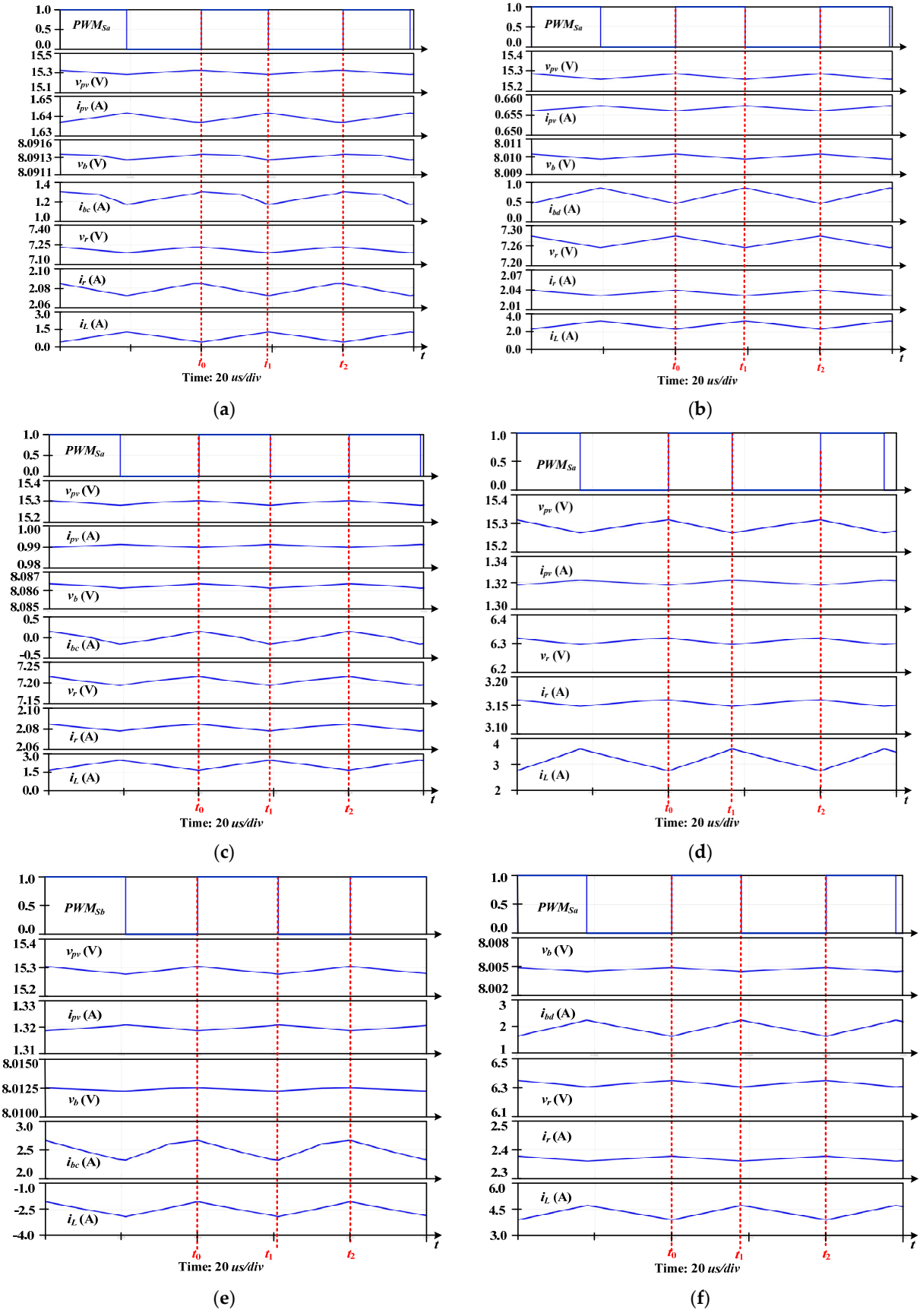

Figure 13. Simulation key waveforms at steady state operation: (**a**) Mode I; (**b**) Mode II; (**c**) Mode III; (**d**) Mode IV; (**e**) Mode V; and (**f**) Mode VI.

Figure 13f shows an example in which only the battery supplies energy to the load (Mode VI). As can be seen, the peak inductor current reaches 4.7 A with CCM operation.

To validate the simulation results, an experimental prototype has been built. Figure 14 shows the diagram of the laboratory PV system with the proposed topology, in which an electronic load is connected to the load port with the constant power mode. For the tests, the load power is regulated by the manipulation of the electronic load. A control unit is associated with the electronic circuit for generating the gating signals to adjust the duty ratios. The PV voltage and current are detected by the voltage and current sensors, and sent to a central control unit to implement the MPPT algorithm and operation mode selection.

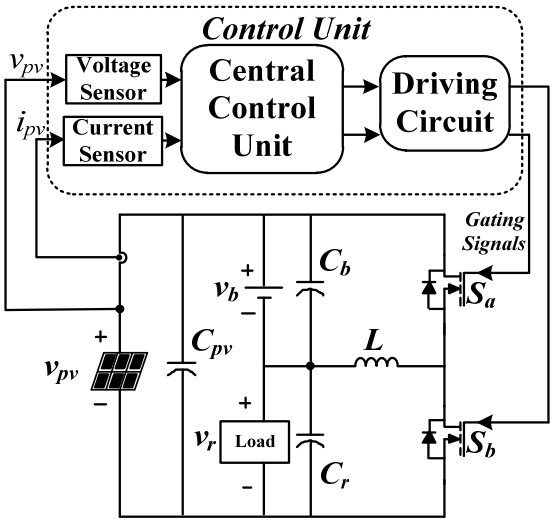

Figure 14. Diagram of the experimental laboratory PV system with the proposed topology and its control unit.

Figure 15 shows a picture of the experimental setup, consisting of a 600 W halogen lamp, a 28 W PV panel, the prototype electronic circuit board, a micro-controller (TEXAS INSTRUMENTS TMS320F28335), a DC power supply, an electronic load, and a battery pack. The circuit and PV parameters are the same as the ones listed in Table 2. The switching frequency is held at 25 kHz and the dead time is set at 0.33 µs, when the power switches change their status.

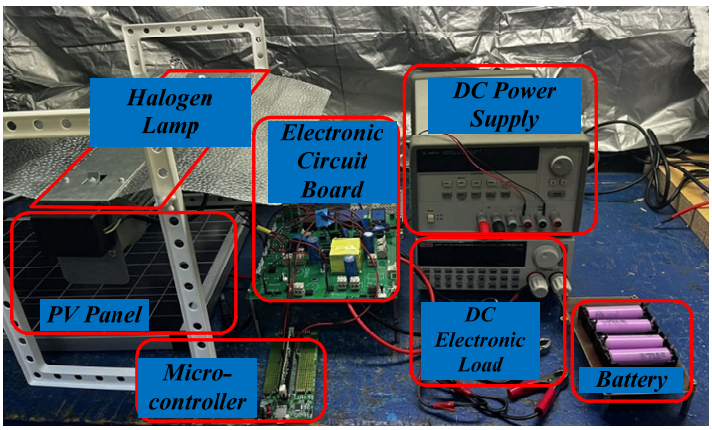

Figure 15. Experimental prototype.

Figures 16–18 show experimental results of the case tests at 1000 W/m^2, 400 W/m^2 and 600 W/m^2, respectively. The SOC of the battery and the load power are held at around 80% and 15 W, respectively. As can be seen in these figures, the PV voltage v_{pv} is regulated

at around the MPP with 15.3 V. The inductor current i_L increases with irradiance from 400 W/m^2 to 1000 W/m^2.

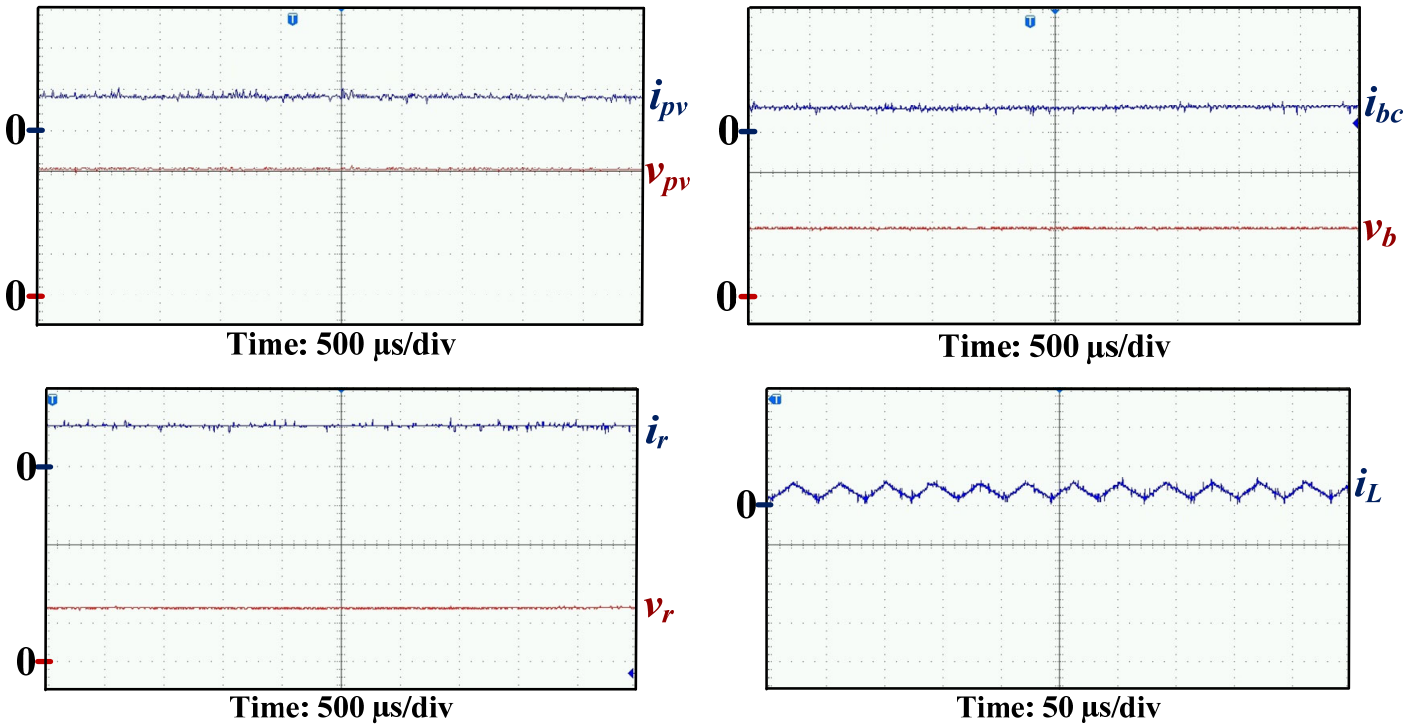

Figure 16. Experimental results when the PV module supplies energy to the load and the battery at 1000 W/m^2. v_{pv}, v_b, v_r, i_{pv}, i_{bc}, i_r, and i_L are shown with 5 V/div and 2 A/div, respectively.

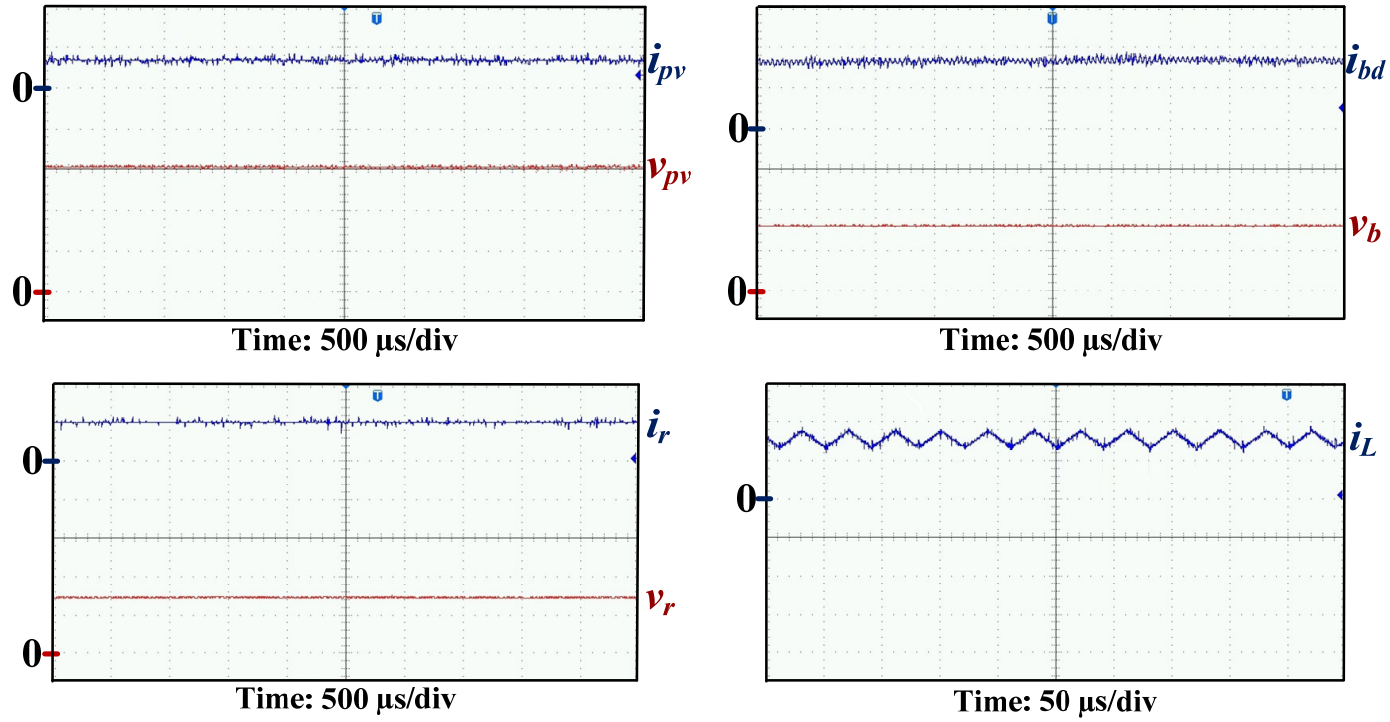

Figure 17. Experimental results when the PV module and battery supply energy to the load at 400 W/m^2. v_{pv}, v_b, and v_r are shown with 5 V/div; i_r and i_L are shown with 2 A/div; and i_{pv} and i_{bd} are shown with 1 A/div.

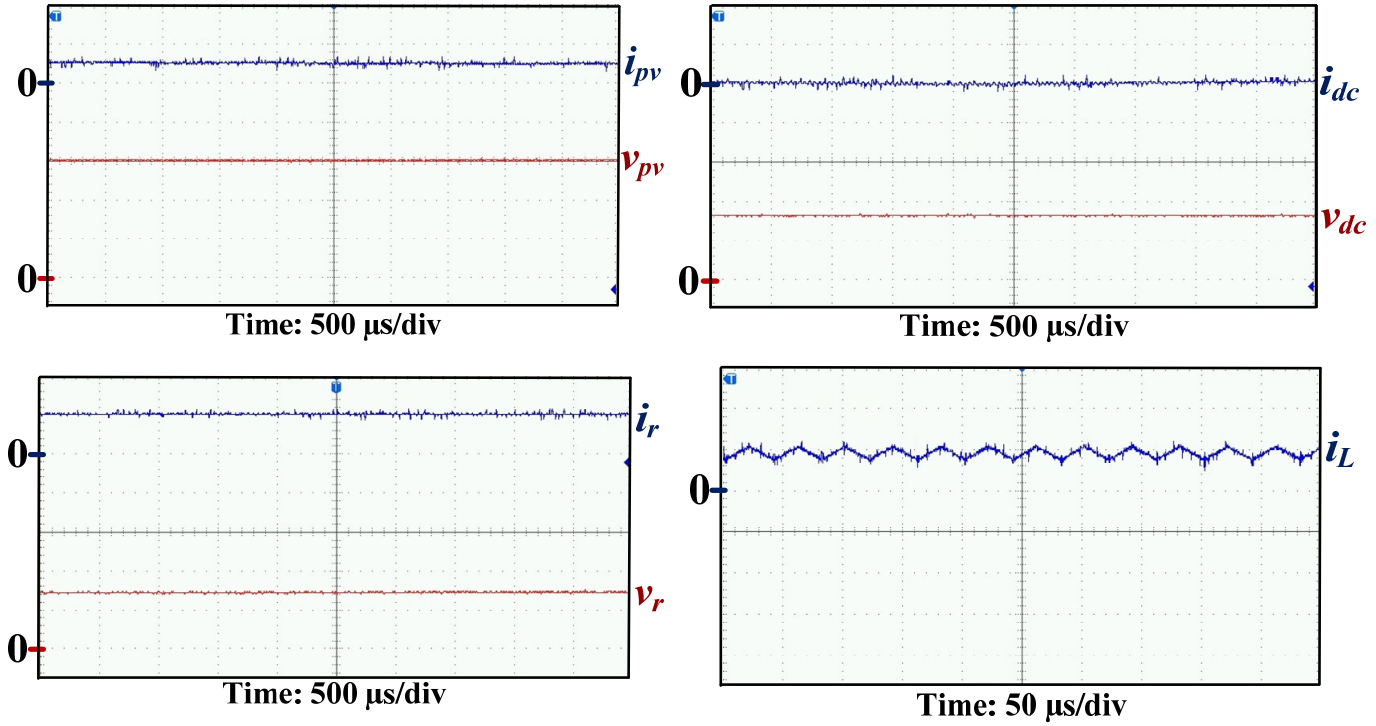

Figure 18. Experimental results when the average PV power is approximately equal to the load power at 600 W/m^2. v_{pv}, v_b, v_r, i_{pv}, i_{bc}, i_r, and i_L are shown with 5 V/div and 2 A/div, respectively.

Figure 19 compiles the results of different tests, including simulation and experimental ones. It shows the simulation and experimental efficiency curves when the PV system is operated at different modes and load powers (10 W, 15 W and 20 W), according to (3), (4), (5), (14) and (15). In the experimental results (solid lines), the irradiance increases from 0 to 1000 W/m^2 with an increase in efficiency from 96.2% to 99.68% (red line) when the load power is at 15 W. Mode III happens when the irradiance is equal to 600 W/m^2. Thus, on the left side of 600 W/m^2, the PV system is operated at Mode II, whereas on the right side of 600 W/m^2, the PV system is operated at Mode I. It also can be found in this figure that, for a given irradiance, the power conversion efficiency increases with the load power. In high irradiance situations, the differences between efficiencies with different load powers decrease. For a given load power (a given color in Figure 19), operation Mode III is remarked. For example, for p_r = 10 W (dark blue line), when the irradiance is at 400 W/m^2, the PV power is approximately equal to the load power with an efficiency of 99.08%. The power conversion efficiency is almost constant when the PV system is operated at Mode IV with an abnormal battery situation, for example, at 98.45% for a load power of 15 W, as shown with the brown line. Figure 19 also illustrates the case of the PV system operated in Mode V. The green line shows that the power efficiency is held at 98.84% for irradiance going from 200 to 1000 W/m^2. As noticed in Figures 16–18, the inductor current increases when the irradiance increases. This means the power processed by the buck–boost converter decreases, resulting in an increase in efficiency (red line in Figure 19).

It can also be seen in Figure 19 that there are some differences between the simulation (dashed lines) and the experimental results in terms of efficiency. This is because the simulation model is mainly aimed at demonstrating the feasibility of the proposal under different conditions, and the losses are simulated in a simple way by the conduction resistance of MOSFETs and the equivalent series resistance of the inductor, R_L. Nevertheless, the efficiency tendency between the simulation and experiment results is similar when the PV system is operated at the same load power and operation point. For simulation results, the highest efficiency is around 99.9% when the circuit is operated at p_r = 10 W and 1000 W/m^2.

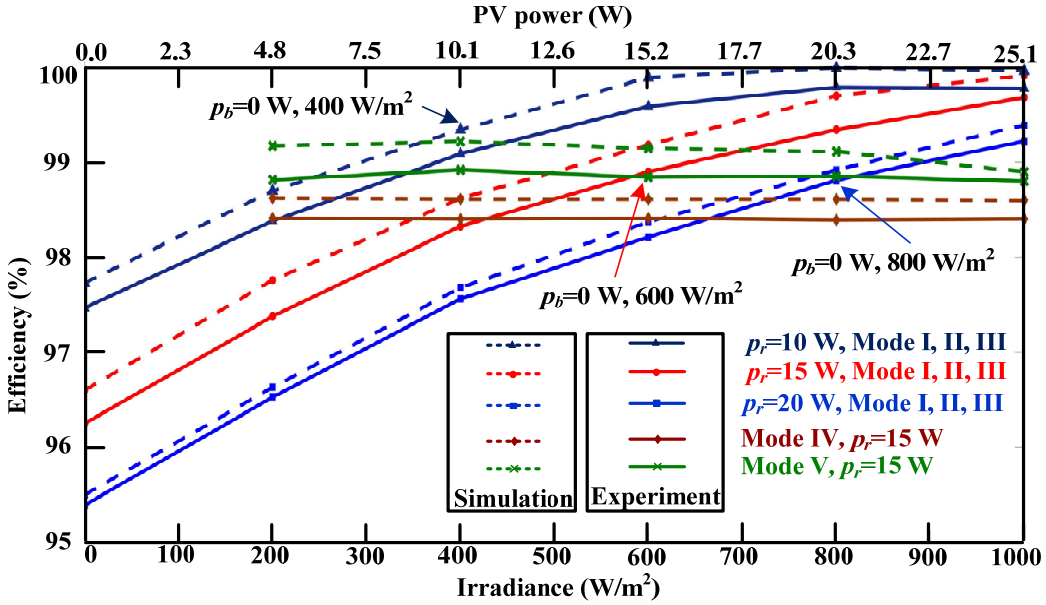

Figure 19. Simulation and experimental efficiency curves when the PV system is operated at different load power and irradiances.

6. Conclusions

A DC-DC converter with partial power regulation for a battery-integrated PV system is proposed. It improves efficiency by implementing PPR in a TPC. A buck–boost converter is connected between the battery and the load to execute the MPPT algorithm. During the battery-charging mode, only a small amount of PV power is processed by the buck–boost converter, resulting in excellent efficiency. During the battery-discharging mode, only two switches and one inductor process the PV power, leading to improved power density.

A PV system with the proposed topology is set up in Simulink and in the laboratory to verify the circuit operation, the effectiveness of a control strategy and the power conversion efficiency. The experimental results illustrate that with partial power technology, the power conversion efficiency of the proposed topology is very high, up to 99.79% in the circuit used as an example.

Author Contributions: Conceptualization, D.Y. and S.M.; Data curation, D.Y.; Formal analysis, D.Y. and S.M.; Funding acquisition, S.M.; Investigation, D.Y.; Methodology, D.Y. and S.M.; Project administration, S.M.; Software, D.Y.; Supervision, S.M.; Validation, D.Y.; Visualization, D.Y.; Writing—original draft, D.Y. and S.M.; Writing—review and editing, D.Y. and S.M. All authors have read and agreed to the published version of the manuscript.

Funding: This research was funded by the Spanish National Research Agency—Agencia Estatal de Investigación, grant number PID2019-108966RB-I00/AEI/10.13039/501100011033.

Data Availability Statement: Data are contained within the article.

Conflicts of Interest: The authors declare no conflicts of interest.

References

1. Chandrasekar, B.; Nallaperumal, C.; Dash, S.S. A Non-isolated Three-Port DC–DC Converter with Continuous Input and Output Currents Based on Cuk Topology for PV/Fuel Cell Applications. *Electronics* **2019**, *8*, 214. [CrossRef]
2. Wang, Z.; Luo, Q.; Wei, Y.; Mou, D.; Lu, X.; Sun, P. Topology Analysis and Review of Three-Port DC–DC Converters. *IEEE Trans. Power Electron.* **2020**, *35*, 11783–11800. [CrossRef]
3. Dobakhshari, S.S.; Fathi, S.H.; Milimonfared, J. A New Soft-Switched Three-Port DC/DC Converter with High Voltage Gain and Reduced Number of Semiconductors for Hybrid Energy Applications. *IEEE Trans. Power Electron.* **2020**, *35*, 3590–3600. [CrossRef]
4. Wang, L.; Wang, H.; Fu, M.; Liang, J.; Liu, Y. A Three-Port Energy Router for Grid-Tied PV Generation Systems with Optimized Control Methods. *IEEE Trans. Power Electron.* **2023**, *38*, 1218–1231. [CrossRef]

5. Wang, G.; Wen, H.; Xu, P.; Liu, W.; Zhou, J.; Yang, Y. A Comprehensive Review of Integrated Three-Port DC–DC Converters with Key Performance Indices. *IEEE Trans. Power Electron.* **2024**, *39*, 6391–6408. [CrossRef]
6. Zhang, B.; Wang, P.; Bei, T.; Li, X.; Che, Y.; Wang, G. Novel topology and control of a non-isolated three port DC-DC converter for PV-battery power system. In Proceedings of the 2017 20th International Conference on Electrical Machines and Systems (ICEMS), Sydney, Australia, 11–14 August 2017.
7. Meshael, H.; Elkhateb, A.; Best, R. Topologies and Design Characteristics of Isolated High Step-Up DC–DC Converters for Photovoltaic Systems. *Electronics* **2023**, *12*, 3913. [CrossRef]
8. Teymour, H.R.; Sutanto, D.; Muttaqi, K.M.; Ciufo, P. Solar PV and battery storage integration using a new configuration of a three-level NPC inverter with advanced control strategy. *IEEE Trans. Energy Convers.* **2014**, *29*, 354–365.
9. Tao, H.; Duarte, J.L.; Hendrix, M.A.M. Multiport converters for hybrid power sources. In Proceedings of the IEEE Power Electronics Specialists Conference, Rhodes, Greece, 15–19 June 2008.
10. Zhu, Y.; Yao, J.; Wu, D. Comparative study of two stages and single stage topologies for grid-tie photovoltaic generation by PSCAD/EMTDC. In Proceedings of the 2011 International Conference on Advanced Power System Automation and Protection, Beijing, China, 16–20 October 2011.
11. Hamed, H.A.; Abdou, A.F.; Acharya, S.; El Moursi, M.S.; El-Kholy, E.E. A novel dynamic switching table based direct power control strategy for grid connected converters. *IEEE Trans. Energy Convers.* **2018**, *33*, 1086–1097. [CrossRef]
12. Zhang, N.; Sutanto, D.; Muttaqi, K.M. A review of topologies of three-port DC–DC converters for the integration of renewable energy and energy storage system. *Renew. Sustain. Energy Rev.* **2016**, *56*, 388–401. [CrossRef]
13. Bhattacharya, S.; Samanta, S. A novel non-isolated three-port DC–DC converter for photovoltaic applications. In Proceedings of the 2020 IEEE International Conference on Power Electronics, Smart Grid and Renewable Energy (PESGRE2020), Cochin, India, 2–4 January 2020.
14. Monteiro, V.; Pinto, J.G.; Afonso, J.L. Experimental validation of a three-port integrated topology to interface electric vehicles and renewables with the electrical grid. *IEEE Trans. Ind. Informat.* **2018**, *14*, 2364–2374. [CrossRef]
15. Qian, Z.; Abdel-Rahman, O.; Al-Atrash, H.; Batarseh, I. Modeling and control of three-port DC/DC converter interface for satellite applications. *IEEE Trans. Power Electron.* **2010**, *25*, 637–649. [CrossRef]
16. Krishnaswami, H.; Mohan, N. Three-port series resonant DC-DC converter to interface renewable energy sources with bidirectional load and energy storage ports. *IEEE Trans. Power Electron.* **2009**, *24*, 2289–2297. [CrossRef]
17. Wu, Y.-E.; Chiu, P.-N. A High-Efficiency Isolated-Type Three-Port Bidirectional DC/DC Converter for Photovoltaic Systems. *Energies* **2017**, *10*, 434. [CrossRef]
18. Wang, C.-S.; Li, W.; Wang, Y.-F.; Han, F.-Q.; Meng, Z.; Li, G.-D. An isolated three-port bidirectional DC-DC converter with enlarged ZVS region for HESS applications in DC microgrids. *Energies* **2017**, *10*, 446. [CrossRef]
19. Zeng, J.; Qiao, W.; Qu, L. An Isolated Three-Port Bidirectional DC–DC Converter for Photovoltaic Systems with Energy Storage. *IEEE Trans. Ind. Appl.* **2015**, *51*, 3493–3503. [CrossRef]
20. Wang, K.; Gao, N.; Wu, W. An Isolated Three-Port DC-DC Converter with a Current-Fed Half-Bridge Port for Battery Energy Storage System. In Proceedings of the 2023 2nd Asia Power and Electrical Technology Conference (APET), Shanghai, China, 28–30 December 2023.
21. Wu, H.; Jia, Y.; Yang, F.; Zhu, L.; Xing, Y. Two-Stage Isolated Bidirectional DC–AC Converters with Three-Port Converters and Two DC Buses. *IEEE J. Emerg. Sel. Top. Power Electron.* **2020**, *8*, 4428–4439. [CrossRef]
22. Rastogi, P.; Bhat, A. Partially Isolated Three-Port Quasi-Switched-Boost Integrated LCL-T Converter for DC Micro-Grids. In Proceedings of the 2021 IEEE 2nd International Conference on Smart Technologies for Power, Energy and Control (STPEC), Bilaspur, India, 19–22 December 2021.
23. Sun, X.; Shen, Y.; Li, W. A novel LLC integrated three-port DC-DC converter for stand-alone PV/battery system. In Proceedings of the 2014 IEEE Conference and Expo Transportation Electrification Asia-Pacific (ITEC Asia-Pacific), Beijing, China, 31 August–3 September 2014.
24. Taheri, S.M.; Baghramian, A.; Pourseyedi, S.A. A Novel High-Step-Up SEPIC-Based Nonisolated Three-Port DC–DC Converter Proper for Renewable Energy Applications. *IEEE Trans. Power Electron.* **2023**, *70*, 10114–10122. [CrossRef]
25. Zhang, Y.; Li, S.; Wang, Y.; Wang, J.; Chen, Z.; Huang, Y. A Two-Switch SEPIC-Based Nonisolated Three-Port Converter Featuring High Step-Up Gain for Solar PV Applications. *Electronics* **2023**, *12*, 1712. [CrossRef]
26. Cheng, T.; Lu, D.D.C.; Qin, L. Non-Isolated Single-Inductor DC/DC Converter with Fully Reconfigurable Structure for Renewable Energy Applications. *IEEE Trans. Circuits Syst. II Express Briefs* **2018**, *65*, 351–355. [CrossRef]
27. Moradisizkoohi, H.; Elsayad, N.; Mohammed, O.A. A Family of Three-Port Three-Level Converter Based on Asymmetrical Bidirectional Half-Bridge Topology for Fuel Cell Electric Vehicle Applications. *IEEE Trans. Power Electron.* **2019**, *34*, 11706–11724. [CrossRef]
28. Nair, S.S.; Rajeev, M. A Novel High Gain Non-Isolated Three-port Converter for Stand-Alone PV Applications. In Proceedings of the 2023 International Conference on Computer, Electronics & Electrical Engineering & their Applications (IC2E3), Srinagar Garhwal, India, 8–9 June 2023.
29. Liang, T.-J.; Tran, T.A.A.; Huynh, K.K.N.; Chen, K.-H. Soft-Switching Three-Port Converter with a Three-Winding Coupled Inductor. *IEEE J. Emerg. Sel. Top. Power Electron.* **2023**, *11*, 5470–5485. [CrossRef]

30. Moo, C.S.; Chen, Y.J.; Yang, W.C. An Efficient Driver for Dimmable LED Lighting. *IEEE Trans. Power Electron.* **2012**, *27*, 4613–4618. [CrossRef]
31. Jeong, H.; Lee, H.; Liu, Y.; Kim, K. Review of Differential Power Processing Converter Techniques for Photovoltaic Applications. *IEEE Trans. Energy Convers.* **2019**, *34*, 351–360. [CrossRef]
32. Xue, L.; Shen, Z.; Boroyevich, D.; Matavelli, P.; Diaz, D. Dual active bridge-based battery charger for plug-in hybrid electric vehicle with charging current containing low frequency ripple. *IEEE Trans. Power Electron.* **2015**, *30*, 7299–7307. [CrossRef]